



## ORIGINAL ARTICLE

# Fractal features of pH-sensitive bimodal mesoporous silica-supported bipyridine-proline organocatalysts with core-shell structure and their application in asymmetric aldol reaction



Guangpeng Xu, Bingying Jia, Bang Xu<sup>\*</sup>, Shiyang Bai, Jihong Sun<sup>\*</sup>, Tallat Munir

Beijing Key Laboratory for Green Catalysis and Separation, Department of Chemical Engineering, Beijing University of Technology, 100 PingLeYuan, Chaoyang District, Beijing 100124, PR China

Received 20 October 2022; accepted 22 April 2023

Available online 26 April 2023

## KEYWORDS

Asymmetric aldol reaction;  
Bimodal mesoporous silicas;  
Bipyridine-proline;  
Fractal characteristic;  
pH-sensitive

**Abstract** Using poly(acrylic acid) (abbreviated as PAA) as a shell, bimodal mesoporous silicas (abbreviated as BMMs) as a core, and bipyridine-proline (abbreviated as Z) as an active species, a facile approach for preparation of the P-Z@BMMs nanocomposites with core-shell structure was proposed, which was used as a suitable pH-sensitive catalyst for asymmetric aldol reaction between p-nitrobenzaldehyde and cyclohexanone. Their microstructural features and physicochemical properties were extensively characterized by various methods, such as powder X-ray diffraction patterns, N<sub>2</sub> adsorption-desorption isotherms, the scanning (and transmission) electron microscopy images, the dynamic light scattering measurements, the thermogravimetric analysis, the elemental analysis, and the Fourier transform infrared spectroscopy spectra. Particularly, their fractal evolution, the pair distance distribution function, and the Porod plots were demonstrated via the small-angle X-ray scattering patterns. The results elucidated that the PAA was successfully incorporated onto the external amino-modified surfaces of the mesoporous BMMs, and the particles having PAA grafted thereon had a pH-responsive shell in thickness of around 0.97 nm for controlled release of Z species by adjusting pH value of the reaction medium. Besides, the synthesized P-Z@BMMs presented the satisfactory catalytic yields (around 80%) in comparison with the homo- and heterogeneous catalytic system using Z or Z@BMMs as the catalysts.

© 2023 The Author(s). Published by Elsevier B.V. on behalf of King Saud University. This is an open access article under the CC BY license (<http://creativecommons.org/licenses/by/4.0/>).

<sup>\*</sup> Corresponding authors.

E-mail addresses: [xubang@bjut.edu.cn](mailto:xubang@bjut.edu.cn) (B. Xu), [jhsun@bjut.edu.cn](mailto:jhsun@bjut.edu.cn) (J. Sun).

Peer review under responsibility of King Saud University. Production and hosting by Elsevier.



## 1. Introduction

The direct catalytic asymmetric aldol reaction has gained popularity as an expeditious and straightforward method of accessing enantioenriched  $\beta$ -hydroxycarbonyl compounds in synthetic organic chemistry (Alcaide et al., 2002; Bao et al., 2015). Early landmark studies of List and Barbas (in 2000) firstly reported the proline as a homogeneous catalyst for direct asymmetric aldol reaction between acetone and isobutyraldehyde with satisfactory catalytic activity (up to 97% yield) under the reaction of organic solvent systems (List and Barbas., 2000). Thereafter, proline and its derivatives have played a critical role in the developments of the field of asymmetric catalysis in the last two decades (Vishnumaya and Singh, 2009), owing to their merits of high catalytic efficiency and atomic economy, as well as mild reaction conditions, environmental friendliness and high selectivity.

In particular, a lots of biaryl-based chiral organocatalysts as efficient catalysts have been designed and synthesized for catalytic asymmetric aldol reaction until the recent two decades, among them, similar studies were performed by our collaborators (Zhao et al., 2012; 2013a; 2013b; 2014), which developed a number of bifunctional organocatalysts based on 2,2'-bipyridine skeleton using L-proline as a chiral source for direct asymmetric aldol reactions between *p*-nitrobenzaldehyde and cyclohexanone in aqueous media under the homogeneous system, showing up to 63% yield, 80% enantioselectivities (*ee*), and 93:7 diastereoselectivities (*dr*).

However, most of these above studies were performed under the homogeneous system, and thus the exploration of high-performance heterogeneous catalysts is highly desired keeping in view their higher stability and recyclability (Corma; 2016; Yan and Wang, 2009).

However, immobilization and recycling of L-proline have received considerable concerns and the commonly used insoluble supports for the immobilizations of proline and its derivatives, such as polymers (Lu et al., 2011; Zhou et al., 2017), silicas (Calderón et al., 2005; Dhar et al., 2003; Doyagüez et al., 2007; Gao et al., 2009a; Hsiao et al., 2009; Li et al., 2019; Sánchez-Antonio et al., 2020), and metal-organic frameworks (Kutzscher et al., 2016). Among them, the ordered mesoporous silica materials (such as MCM-41 (Calderón et al., 2005; Dhar et al., 2003; Doyagüez et al., 2007), and SBA-15 (Gao et al., 2009a; Hsiao et al., 2009) have regarded as the promising supports for organocatalysts owing to their extremely large surface area and pore volume, uniform and stable structure, especially easy functionalization. Therefore, several heterogeneous proline-immobilized catalysts have been explored presently. For example, Fernández-Mayoralas et al (Calderón et al., 2005; Doyagüez et al., 2007) proposed a new heterogeneous catalyst for asymmetric aldol reaction between hydroxyacetone and *p*-nitrobenzaldehyde by anchoring proline on functionalized MCM-41 via a post-synthetic modification method, showing excellent catalytic performance (up to 99% *ee*). Gao et al. (Gao et al., 2009a) immobilized proline derivatives onto the surface of SBA-15, affording the satisfactory yield (up to 87%) and 90% *ee* for asymmetric aldol reaction between cyclohexanone and *p*-nitrobenzaldehyde under low-temperature conditions.

Comparably, our research group (in 2003) firstly proposed the multifunctional bimodal mesoporous SiO<sub>2</sub> (BMMs) as suitable support with high loading capacity and further achieved excellent significance effect on in the catalytic and drug delivery systems, owing to their higher specific surface area (> 700 m<sup>2</sup>/g), large pore volume (up to 3.5 cm<sup>3</sup>/g), as well as adjustable bimodal size distributions and modifiable surface properties, in which, the nearly spherical shape of BMMs particles with the uniform small mesopores around 3 nm, and the large mesopores around 15–50 nm (Sun et al., 2003). Compared with the highly oriented MCM-41 and SBA-15 materials, the availability of a large amount of short worm-like channels and abundant hydroxyl in the disordered structures of the BMMs provide various surface-functionalized possibilities via covalent or noncovalent bonds. Therefore, based on our previous studies with this motivation, various

heterogeneous proline-immobilized catalysts with high activities were explored via hydrogen bond or coordination bond method (Sun et al., 2018; Tang et al., 2018; Xu et al., 2020; 2021; 2022; Zhang et al., 2019) showing a higher catalytic activity for asymmetric aldol reaction between cyclohexanone and various aldehyde derivatives in comparison with that of homogeneous catalysts.

Nevertheless, on the one hand, the aggregation of particles often caused poor dispersion of the active species on the inner-surface of silica during preparation process. Thereby, surface treatments with organic groups are beneficial to provide a good dispersity, meanwhile, the coating is conducive to avoid particle aggregation (Suzuki et al., 2000). On the other hand, controllable active species releasing from the support still failed to be achieved under the above heterogeneous systems, despite the heterogeneous catalyst can be reused for several cycles. Thus, developing a simple and efficient strategy that can realize controllable guest molecules release by altering the external conditions is highly warranted. pH is one of the most important stimuli to trigger and modulate the release of loaded active species from support. Therefore, the synthesis of the pH-sensitive catalyst with satisfactory catalytic performance is one of the crucial research goals in this work. Comparably, its obvious advantages over the above two compared homo- and heterogeneous catalysis systems.

Recently, poly(acrylic acid) (PAA) and their derivatives have been demonstrated to be the representative pH-sensitive and biocompatible polymer, this characteristic has been widely utilized in applications of controlled drugs release (Gao et al., 2009b; Hong et al., 2009; Suzuki et al., 2000; Tan et al., 2015; Yuan et al., 2011; Ye and Lay, 2013; Zhou et al., 2018), enzyme immobilization (Esmailnejad-Ahranjani et al., 2016), and many other fields. In which, Suzuki et al (Suzuki et al., 2000) initially evaluated the feasibility of grafting PAA on the surface of porous silica via covalent bonds. Hong et al. (Hong et al., 2009) designed the pH-responsive nanomaterials with core-shell structures by grafting PAA on the surface of mesoporous silica, using reversible addition-fragmentation chain transfer (RAFT) polymerization. Subsequently, an intelligent system was performed to encapsulate doxorubicin in a novel nanocontainer to obtain a pH-responsive drug release (Zhou et al., 2015). Besides, a facile approach was developed by Arpanaei et al. that the preparation of core-shell structured PAA-coated Fe<sub>3</sub>O<sub>4</sub> cluster@SiO<sub>2</sub> nanocomposite particles as the support materials for the lipase immobilization (Esmailnejad-Ahranjani et al., 2016). Besides that, our research group also carried out a series of relevant studies around the synthesis and application of pH-sensitive polymer (Jin et al., 2018; Han et al., 2015; Ma et al., 2020; Xu et al., 2022b; Wang et al., 2017). In essence, most studies so far have concentrated on the exploration of the drug loading and releasing behaviors. However, few studies focused on the controlled release of chiral organocatalyst using pH-sensitive composites as useful support for the catalytic asymmetric aldol reaction have been reported over the past few years in literature. Accordingly, one of the main novelties and contributions of the present work is to fabricate a pH-sensitive hybrid catalyst that achieved high catalytic performance through controlling the guest molecules release.

Herein, the pH-sensitive hybrid catalyst (P-Z@BMMs) with core-shell feature based on BMMs as a core and PAA as a shell was prepared via a covalent attachment approach, this strategy comprises allowing the carboxyl group of the PAA and an amino group on the surface of BMMs to undergo a coupling reaction under the action of activator (EDCI/NHS), covalently coating the polymer to the silica surface, afterwards loading the bipyridine-proline organocatalyst into the mesoporous channels of pre-synthesized PAA-coated BMMs, thereby the synthesis of stimuli-responsive catalyst was demonstrated through the controlled release of Z species. In which, the (*S*)-*N*-(3'-(*n*-aphthalene-1-sulfonamido)-[2, 2'-bipyridin]-3-yl) pyrrolidine-2-carboxamide (abbreviated as Z) as active species were first synthesized by our group (Xu et al., 2022a), which presented satisfactory catalytic efficiency for various asymmetric aldol reactions under the homo- and heterogeneous systems.

Most importantly, how to prove that whether the PAA shells are indeed coated onto the surface of the BMMs core remains one of a thorny problem. For this purpose, the small-angle X-ray scattering (SAXS) method were introduced to address above issues in this work. It is well known that the SAXS technique offer alternative solutions to achieve non-destructive and high sensitivity various porous (Hammersley et al., 2016; Li et al., 2001; Svergun et al., 2003) or polymers detections (Jin et al., 2018; Ma et al., 2020; Xu et al., 2022; Wang et al., 2017). In which, this technique has been successfully applied for functionalizing the mesoporous silicas by many researchers (Hammersley et al., 2016; Li et al., 2001; Svergun et al., 2003). Therefore, based on these encouraging studies, the SAXS method (such as the fractal dimension, the characteristic shape and size, and the thickness of the interfacial layer) combined with other characterizations for elucidation of the microstructural properties of above pH-sensitive composites were particularly proposed in the present work, in which, not only the fractal dimensions of above hybrid materials before and after modification was elucidated derived from the integrated scattering curves, but also the pore geometries and particle morphologies on the basis of the pair distance distribution function ( $P(r) \sim r$ ) (PDDF) profiles, and the thickness of interfacial layer (polymer shell) was determined by Porod plot. Another novelty and contribution of this investigation is that the feasibility of preparation of the core-shell structured polymer-coated composites was particularly demonstrated by SAXS analysis combined with other characterizations. Meanwhile, the essential influences of pH-sensitive catalyst on the catalytic activities and stereoselectivities of the asymmetric aldol reaction between *p*-nitrobenzaldehyde and cyclohexanone under various pH conditions were preliminarily explored as well. Furthermore, the microstructural features and physicochemical properties of all samples were extensively characterized by means of the powder X-ray diffraction (XRD) patterns,  $N_2$  adsorption-desorption isotherms, the scanning (and transmission) electron microscopy (SEM and TEM), the dynamic light scattering (DLS) measurements, the thermogravimetric analysis (TGA) curves, the elemental analysis, and the Fourier transform infrared spectroscopy (FT-IR) spectra. In particular, the analysis of asymmetric aldol reactions products was determined by high-performance liquid chromatography (HPLC).

## 2. Experimental section

### 2.1. Chemicals

Tetraethyl orthosilicate (TEOS, 98%) and 3-aminopropyltriethoxysilane (APTES, 98%) were purchased from Bailingwei Technology Beijing Co., Ltd. Cetyltrimethylammonium bromide (CTAB, 99% of purity) was purchased from Sinopharm Chemical Reagent Beijing Co., Ltd. Anhydrous ethanol (99%), toluene (99%), sodium sulfate ( $Na_2SO_4$ , 99.5%), and ammonium hydroxide (25%,  $NH_4OH$ ) were obtained from Beijing chemical works. Polyacrylic acid (PAA, average molecular weights of 2000) was purchased from Shanghai Macklin Biochemical Co., Ltd. 1-(3-dimethylamino propyl)-3-ethylcarbodiimide hydrochloride (EDCI, 99%) was purchased from Shanghai Saen Chemical Technology Co., Ltd. N-Hydroxysuccinimide (NHS, 99%) was purchased from Shanghai Yuanye Bio-Technology Co., Ltd. Ethanol (GC, 98%), *n*-Hexane (GC, 98%), ammonium nitrate ( $NH_4NO_3$ , 98%), and *p*-nitrobenzaldehyde (99.8%) were supplied by Shanghai Aladdin Biochemical Technology Co., Ltd. *N,N*-dimethylformamide (DMF, 99%), petroleum ether (60–90 °C), ethyl acetate (EtOAc, 99.9%), dichloromethane ( $CH_2Cl_2$ , 99.9%), trifluoroacetic acid (TFA, 99.9%), sodium

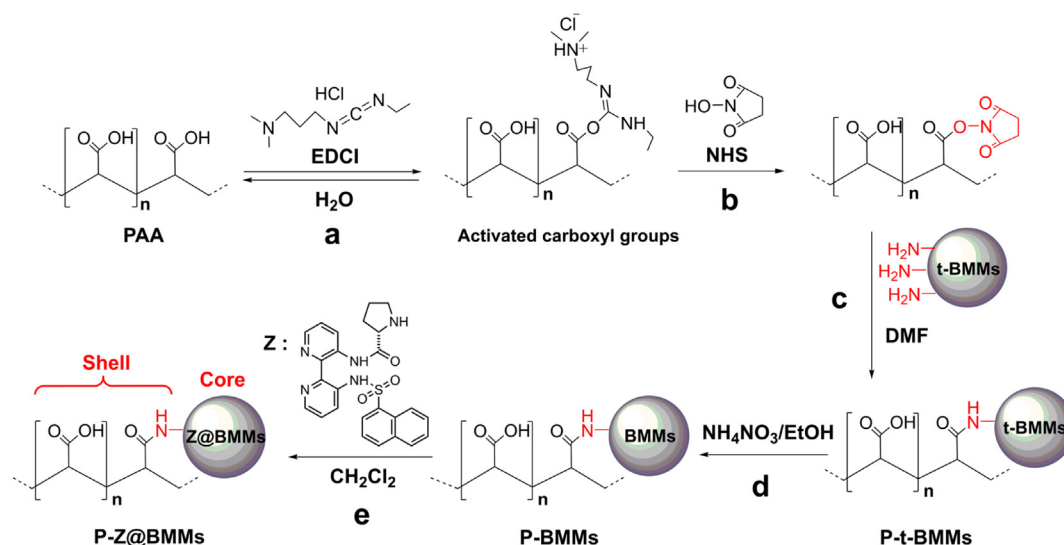
hydroxide, and cyclohexanone (99.9%) were provided by Tianjin Fuchen chemical reagents factory. 0.25 mm SDS silica gel coated glass plates (60F254) and silica gel (200–300 mesh) were purchased from Qingdao Haiyang Chemical Co., Ltd. All chemicals were obtained as reagent grade and used without further purification. All of the solvents and reagents were of A.R. grade, unless otherwise noted. Deionized water was used in all experiments.

### 2.2. Synthesis of pH-sensitive catalyst

The synthesis routes of pH-sensitive hybrid catalyst (P-Z@BMMs) with core-shell nanostructures are demonstrated, as shown in Scheme 1.

Due to the weak acylating properties of carboxylic groups, EDCI/NHS coupling systems were used. Herein, EDCI was used to activate the terminal carboxyl groups on the PAA chains for conjugation with primary amines of template-contained BMMs (as shown in Scheme 1a), and NHS was used to improve the efficiency of EDCI-mediated coupling reactions by stabilization of the amine-reactive intermediate (as shown in Scheme 1b and c) (Wang et al., 2011). Particularly, the CTAB templates were removed by  $NH_4NO_3$ /EtOH solutions, the advantages of worm-like mesoporous structures of BMMs was highlighted (as shown in Scheme 1d). Then, the Z species were able to be loaded into PAA-coated BMMs (as shown in Scheme 1e). The synthesis procedure of BMMs with template (CTAB) was partially based on the method reported by Sun et al. (Sun et al., 2003). In details: 2.62 g CTAB was dissolved in 105 mL distilled water and stirred magnetically until it was completely dissolved, 8.0 mL of TEOS was then added drop-wise to the abovementioned solution. Subsequently, 3.5 mL of  $NH_4OH$  (25%) was quickly injected into the solution. After stirring for about 10 min at room temperature, the solution turned into white gels. The precipitate was filtrated and thoroughly washed with distilled water, and finally dried overnight at 80 °C under vacuum, the resulting product was named as t-BMMs. The sample (0.5012 g) of t-BMMs was weighted and transported into a 100 mL round-bottom flask, and then dehydrated in vacuum oven at 120 °C for 3 h before using. Subsequently, the dried sample was dispersed into anhydrous toluene solution (20 mL) and 0.5 mL of APTES was added drop-wise under magnetic stirring, then placed in an oil bath at 110 °C for 12 h. After centrifuged, the resultant precipitates were collected and washed with absolute ethanol, then dried at 60 °C for 6 h. The resulting product was named as t-BMMs-APS.

As shown in Scheme 1a and b, to activate the carboxyl groups of PAA, 20 mg of PAA was dissolved into 20 mL DMF solution and heated at 80 °C for 0.5 h under magnetic stirring. Then, the corresponding amount of EDCI and NHS were added sequentially according to the molar ratio of EDCI/NHS = 4:1, the mixture was subsequently stirred for 1 h. As shown in Scheme 1c, the dried sample of t-BMMs-APS (150 mg) was added to the above solution and continually stirred for 6 h. After that, the solid was separated from the liquid phase by centrifugation, washed alternately by distilled water and ethanol, and dried at 80 °C for 6 h. The resultant composite nanoparticles were named as P-t-BMMs.



**Scheme 1** The synthesis routes of the pH-sensitive catalyst (P-Z@BMMs).

As shown in [Scheme 1d](#), the P-t-BMMs (100 mg) was dispersed in 10 mL of the prepared 10 mg/mL  $\text{NH}_4\text{NO}_3/\text{EtOH}$  solutions, then the reaction mixture was heated at 80 °C under reflux for 12 h, and repeated for three times, the CTAB was removed through washing as described above. After that, the solid was centrifuged, washed alternately by distilled water and ethanol, then dried at 80 °C for 6 h. The obtained products were named as P-BMMs.

The active species (Z) was synthesized according to our previously reported literature procedure ([Xu et al., 2020](#)), the Z loading was carried out as follows. As shown in [Scheme 1e](#), the P-BMMs (100 mg) was dispersed in 10 mL of  $\text{CH}_2\text{Cl}_2$  solution containing 50 mg of Z, and heated at 42 °C for 8 h under magnetic stirring. After that, the mixture solution was centrifuged, the obtained precipitate was washed alternately by  $\text{CH}_2\text{Cl}_2$  and ethanol, dried at 80 °C for 8 h. The resultant pH-sensitive catalysts were named as P-Z@BMMs.

### 2.3. pH-dependent catalytic behaviours

The asymmetric aldol reaction was performed under various pHs (pH = 1.53, 7.21, 8.02, 9.24, and 10.18, respectively). A typical procedure was as follows. Cyclohexanone (1.0 mmol, 104  $\mu\text{L}$ ) was stirred in various pHs solutions (0.5 mL) at room temperature for 5 min. The desired amounts of pH-sensitive catalyst (P-Z@BMMs, 5 mol% of *p*-nitrobenzaldehyde) was added to the above solutions, and stirred for 5 min, then the *p*-nitrobenzaldehyde (0.1 mmol) was added. The mixture solution was constantly stirred for 120 h. The reaction progress was monitored by thin-layer chromatography (TLC system: EtOAc/petroleum ether = 1: 2, v/v), using precoated TLC plates of silica gel 60F254. After that, the solid/liquid was separated by centrifugation, the resultant aqueous solution was extracted with ethyl acetate (3  $\times$  10 mL). The combined organic extracts were dried over anhydrous  $\text{Na}_2\text{SO}_4$ , filtered and concentrated in vacuo. Finally, the crude product was purified by column chromatography on silica gel (eluent: EtOAc/petroleum ether) to afford a mixture of *syn*- and *anti*-

aldol products, and the *dr* and *ee* values were determined by chiral HPLC analysis.

The turnover frequency (TOF) and turnover number (TON) can be described in detail as Eqs. (1) and (2).

$$\text{TOF} = n_1 / (m_1 \times n_2 \times t) \quad (1)$$

$$\text{TON} = n_1 / \text{QUOTE TON} = \frac{n_1}{n_2} n_2 \quad (2)$$

Where  $n_1$  denote the moles of the product molecules,  $n_2$  denote the moles of the involved in catalysis Z,  $m_1$  denote the weight of the used catalyst, and  $t$  denotes the whole catalytic reaction time, respectively.

A simplified scheme of the experimental and research methodology was given in [Scheme S1](#) in the ESI section. Using PAA as a shell and BMMs as a core, PAA was grafted into the surfaces of the BMMs by a facile grafting strategy, the resultant P-BMMs could be used as bipyridine-proline (Z) support, and thereby a novel pH-responsive P-Z@BMMs catalyst was prepared. Hopefully, the catalytic performances for asymmetric aldol reaction presented a high efficiency by adjusting pH value of the reactive media.

### 2.4. Characterizations

The powder XRD patterns were recorded on a D6 Advance X-ray diffractometer (Beijing Pu Analysis General Instrument Co., Ltd, Beijing, China) using Cu-K $\alpha$  radiation ( $\lambda = 0.1540$  56 nm, 36 kV, 20 mA) at a scanning speed of 1° and 4° per min in the 1–10° and 5–50° of 2 $\theta$  range for the experiments, respectively. The textural properties of related samples were determined from  $\text{N}_2$  sorption isotherms measured at 77 K using JWGB JW-BK300 analyzer. Prior to each adsorption measurement the samples were outgassed under vacuum at 353 K for at least 5 h. The specific surface area was calculated using the Brunauer-Emmett-Teller (BET) method and the pore size distribution was calculated from the isotherm using the Barrett-Joyner-Halenda (BJH) model. Besides that, the total

pore volume was determined from the N<sub>2</sub> adsorbed amount at a relative vapor pressure ( $P/P_0$ ) of approximately 0.99. The SEM images were performed on a Hitachi field-emission scanning electron microscope (S-4800) with an acceleration voltage of 15.0 kV. The morphology of the materials was acquired with a TEM microphotograph (JEOL, JEM-2100F, Japan). The DLS measurements was performed using Zetasizer (Malvern, Herrenberg, Germany). The TGA was carried out on a PerkinElmer Simultaneous Thermal Analyzer (STA-8000) instrument from 30 to 900 °C at a heating rate of 10 °C/min under the N<sub>2</sub> atmosphere with a flow rate of 20 mL/min. The content of sulfur was measured by an elemental analyzer (Vario MICRO, Germany). The FT-IR spectra were measured recorded on a Spectrum 100 spectrometer (PerkinElmer, Waltham, MA, USA) via the KBr tablet method, in which the spectral resolution was 4 cm<sup>-1</sup>, and 32 scans were recorded for each spectrum. The dr and ee values were determined by HPLC analyses on an Agilent Technologies 1200 system equipped with a photodiode array detector, using Chiralpak AD-H column (25 cm × 0.46 cm) by Daicel Chemical Ind., Ltd (Detection: UV 254 nm, flow rate: 1.0 mL/min, injection: 5.5 μL, mobile phase: n-Hexane/Ethanol). Besides that, the chemical identity of the bipyridine-proline catalyst (Z) and aldol products has been confirmed by nuclear magnetic resonance (<sup>1</sup>H- or <sup>13</sup>C NMR) in our previous report (Xu et al., 2020).

In particular, the SAXS experiments were carried out using synchrotron radiation at the 1W2A X-ray beamline at Beijing Synchrotron Radiation Facility (BSRF). The wavelength of the incident X-ray was 0.154 nm. The sample-to-detector distance for SAXS was 1.59 m, calibrated with the diffraction ring of a standard sample. The scattering vector magnitude  $q$  ranged from 0.08 to 3.05 nm<sup>-1</sup> for the experiment reported in this paper. The intensity of scattering,  $I(q)$  was measured as a function of  $q$ , where  $q$  was considered as  $4\pi\sin\theta/\lambda$ . The sample was loaded into a sample cell and sealed with scotch tape on a groove. The thickness of the sample cell was approximately 1 mm. The scattering image was collected with an exposure time of 5 min by the single-frame mode with a ‘multi-read’ of 2 times. The two-dimensional SAXS images were transferred to one-dimensional data by using the Fit2D software (<https://www.esrf.eu/computing/scientific/FIT2D>) (Hammersley, 2016), and further processed with the  $S$  program package (Li et al., 2001). In this study, a slit-collimated beam was used, for which the mass fractals ( $D_m$ ) or surface fractals ( $D_s$ ) were calculated according to the power law.

### 3. Results and discussion

#### 3.1. XRD patterns

The small (1–10°) and wide (5–50°) angle XRD patterns of all synthesized samples are depicted in Fig. 1. As can be seen in Fig. 1A, all samples presented the relatively broad and intense diffraction (100) peaks in the range  $2\theta = 1.5$ –2.5°, indicating a uniform and abundant mesoporous structure, being consistent with previously published literature (Sun et al., 2003).

As shown in Figure S1 in the Electronic Supplementary Information (ESI) section, the t-BMMs exhibited significant decrease in the peak intensity and left-shift in the peak position as compared to the same samples calcinated at 550 °C, suggest-

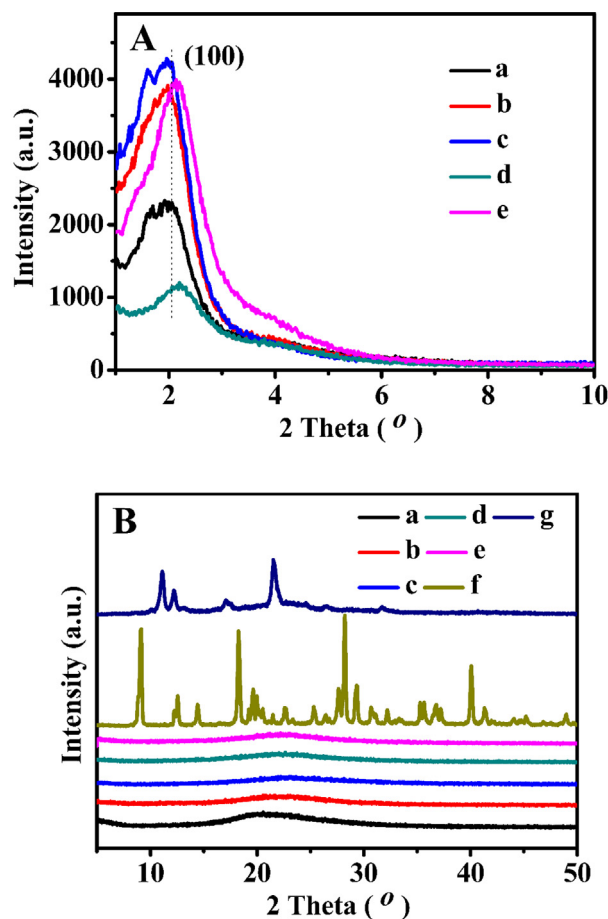


**Fig. 1** Small (A) and wide (B) angle XRD patterns of (a) t-BMMs, (b) t-BMMs-APS, (c) P-t-BMMs, (d) P-BMMs, (e) P-Z@BMMs, (f) PAA, and (g) Z.

ing an enhancement in the degree of ordering of the mesoporous structures during the template removal process. However, the calcinated process for removal of CTAB was accompanied by the shrinkages of the silica frameworks, resulting in a decrease of the crystal plane spacing ( $d$ ) values (Sun et al., 2018; Tang et al., 2018; Xu et al., 2020; 2021; 2022a; Zhang et al., 2019).

As shown in Fig. 1A-a, -b, after surface-modification of the t-BMMs with the silane coupling agents, the intensity of the diffraction peak<sub>(100)</sub> at around 2° was notably enhanced, indicating that the introduction of the amino groups onto the surface of Si-OH was helpful to increase the ordered mesopore regularity. Similarly, comparing the XRD patterns of t-BMMs-APS (as shown in Fig. 1A-b) and PAA-coated t-BMMs (Fig. 1A-c), the intensity of the characteristic peak increased slightly, probable reason was that t-BMMs-APS and P-t-BMMs were further prepared at high temperature, resulting in the improvements of the mesoporous order degree of t-BMMs. However, after further CTAB-removal via heated reflux extraction method, the intensity of diffractive peak<sub>(100)</sub> of P-BMMs (Fig. 1A-d) was lower than that of P-t-BMMs (Fig. 1A-c), one of the main reasons was due to the decreases of the mesoporous order degree of BMMs. Besides that, the peak<sub>(100)</sub> position ( $2\theta$ ) of P-BMMs (Fig. 1A-d) was shifted to a higher angle region, compared with that of P-t-BMMs

(Fig. 1A-c). These observations demonstrate that CTAB was essentially removed by repeated washing, which provided the convenience for active species (Z) immobilization. As shown in Fig. 1A-e, the enhancement in peak<sub>(100)</sub> intensity was observed after Z-immobilization, the peak<sub>(100)</sub> position ( $2\theta$ ) of P-Z@BMMs (Fig. 1A-e) was shifted to a much lower angle region as compared to that of P-BMMs (Fig. 1A-d). These results indicate that the enlarged  $d$  space originates from the successful introduction of Z into the mesoporous channels of PAA-coated BMMs. Meanwhile, it could be evidenced by their pore size distributions and fractal features variations deriving from their  $N_2$  sorption isotherms (as shown in Fig. 2) and SAXS patterns (Fig. 3) in the following section. Additionally, the XRD profiles of all samples (Fig. 1A) showed a typical characteristic diffraction pattern of BMMs, indicating the structural integrity of BMMs-based samples was not destroyed during PAA-grafting and Z-loading.

Noticeably, the wide ( $5\text{--}50^\circ$ ) angle XRD patterns proved the amorphous structure of the prepared BMMs-based materials (as shown in Fig. 1B, from a to e), in which, no differences appeared in their characteristic peak around  $20^\circ$  before and after modification, particularly, no peaks assigned to PAA (Fig. 1B-f) and Z (Fig. 1B-g) were observed. In summary, these observations suggest the uniform coating of PAA over the amino-modified surfaces of BMMs and homogeneous Z-loading on the mesoporous channels of BMMs, thus allowing them to retain their catalytic activity. This forecast can be ensured by the catalytic behaviors discussed in the latter section.

### 3.2. $N_2$ Sorption isotherms

To investigate the pore structures after PAA-grafting or Z-loading,  $N_2$  adsorption-desorption isotherms and the corresponding pore size distributions of all related samples were conducted in Fig. 2. Their collection of the textural parameters and porosity derived from  $N_2$  sorption isotherms are summarized in Table S1. As shown in Fig. 2, the isotherms of all samples were followed the type-IV behaviors with type-H1 hysteresis loops over the whole range of relative pressures (ex-

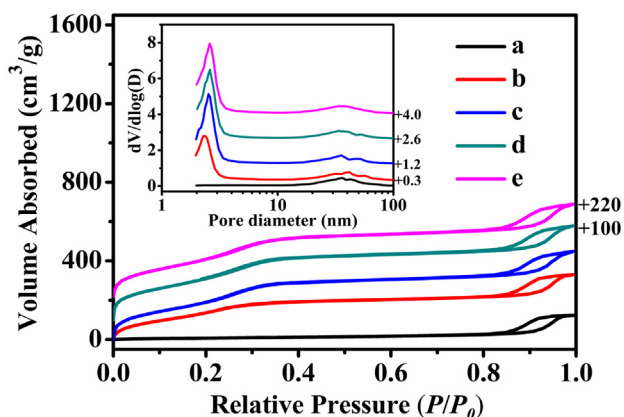


**Fig. 2**  $N_2$  adsorption-desorption isotherms and corresponding pore size distributions (inset) of (a) t-BMMs, (b) t-BMMs-APS, (c) P-t-BMMs, (d) P-BMMs, and (e) P-Z@BMMs. The offset values were remarked in the Y-axis (left).

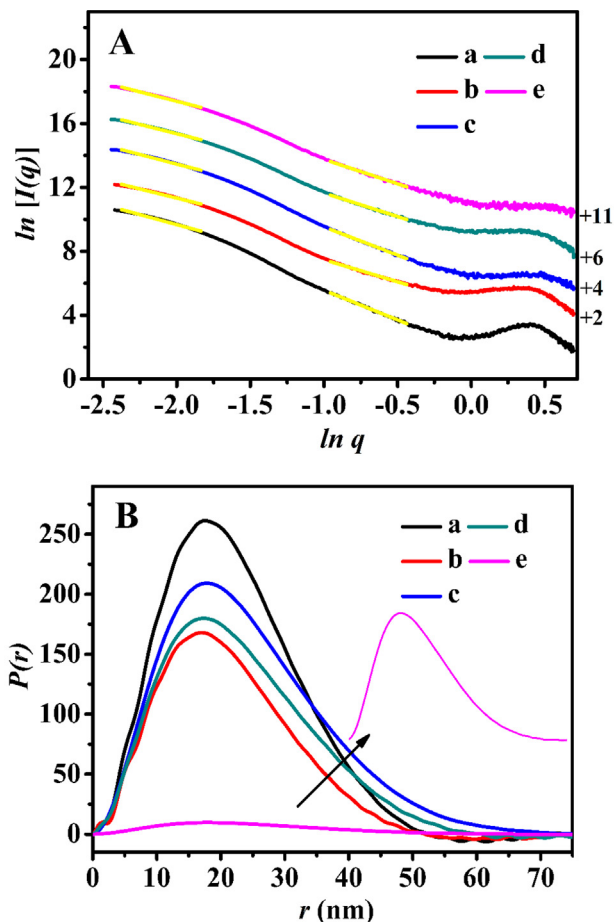


**Fig. 3** (A) Shifted scattering curves (offset values in left Y-axis), and the PDDF profiles (B) of (a) t-BMMs, (b) t-BMMs-APS, (c) P-t-BMMs, (d) P-BMMs, and (e) P-Z@BMMs.

cept Fig. 2a), indicating the presences of the mesoporous structures. Notably, two inflections could be observed in all isotherms (as shown in Fig. 2 from b to e), except for t-BMMs (Fig. 2a) in the low-pressure region. The first hysteresis loops corresponded to a step where the  $N_2$  adsorption within the small pores, besides, the second inflection belonged to the capillary condensation of  $N_2$  within the larger mesopores, being consistent with previously published literature (Sun et al., 2018; Tang et al., 2018; Xu et al., 2020; 2021; 2022a; Zhang et al., 2019).

As shown in Fig. 2 (inset), the pore size distributions were calculated using the Barrett-Joyner-Halenda (BJH) method from the desorption branch of the isotherms. As can be seen in Fig. 2a (inset), the small mesopore of t-BMMs was not be observed, indicating that the structures of t-BMMs was compact with a small specific surface area ( $S_{BET}$ ) and pore volume ( $P_{vol}$ ), the corresponding values were around  $33 \text{ m}^2/\text{g}$ , and  $0.21 \text{ cm}^3/\text{g}$ , respectively. Meanwhile, the large mesopore of t-BMMs was around  $36.15 \text{ nm}$  (Table S1, entry 1), originating from the intra-particle aggregations. As a result of treating with APTES, the amino groups were modified on the surfaces of t-BMMs, the  $S_{BET}$  and  $P_{vol}$  values of t-BMMs-APS (as shown in Fig. 2b (inset) and Table S1, entry 2) were markedly increased to  $642 \text{ m}^2/\text{g}$ , and  $0.60 \text{ cm}^3/\text{g}$ , respectively, especially,

the small mesopores appeared with a sharp peak located at 2.35 nm (Table S1, entry 2), indicating that the partial CTAB located in the mesopores was dissolved. As discussed later, this is compatible with the SAXS demonstrations (as shown in Fig. 3). Besides, after PAA-grafting on the surfaces of t-BMMs-APS, and in turn removal of the CTAB by repetitive organic solvent washing, their  $S_{BET}$  and  $P_{vol}$ , and small mesopore sizes also presented an increasing tendency (Table S1, entries 2–4), in which, the  $S_{BET}$  and  $P_{vol}$ , and small mesopore sizes of P-BMMs were around 913 m<sup>2</sup>/g, 0.83 cm<sup>3</sup>/g, and 2.60 nm (Table S1, entry 4), respectively. However, the  $S_{BET}$  and  $P_{vol}$ , and small mesopore sizes of P-Z@BMMs showed a decreasing trend, showing around 877 m<sup>2</sup>/g, 0.77 cm<sup>3</sup>/g, and 2.59 nm (Table S1, entry 5), respectively. Obviously, one of the main reasons is due to the Z-occupancies in the mesopore channels. Therefore, we speculate the successful linking between –NH<sub>2</sub> and –COOH groups, these findings can be further evidenced with FT-IR spectra in the following discussion.

### 3.3. Saxe analysis

The SAXS patterns of BMMs-based samples are displayed in Fig. 3A, their PDDF curves are presented in Fig. 3B, and their related parameters are summarized in Table 1. As shown in Fig. 3A, the slope of each curve (yellow straight lines) was obtained with a linear fit using the least square method in two distinctive linear regions (low-, or high- $q$  region), and thus the following mass (or surface) fractal dimensions ( $D_m$  or  $D_s$ ) deriving from calculations on the basis of above linear curves are generally determined by power-law decay (Hammersley et al., 2016; Xu et al., 2020; 2021; 2022a). In particular, their variations of the fractal features demonstrate the success of the performed covalent modifications.

As seen in Table 1, the slope values of all related samples were between –2 and –3 in the low- $q$  region ( $0.09 < q < 0.16$ ), their behaviors possessed the  $D_m$  features, corresponding their  $D_m$  values ranged between 2 and 3, indi-

cating that the fractal structures of BMMs-based samples tended to be compact or loose. According to the reported literature (Hammersley et al., 2016; Xu et al., 2020; 2021; 2022a), the increase of  $D_m$  value implies that the fractal structure tends to be closer, otherwise, means that the structure is more open (non-compact), while, the fractal structure of  $D_m = 3$  refers to dense objects.

As listed in Table 1 (entries 1 and 2), the  $D_m$  values slightly decreased after amino-modification, from 2.50 for pure t-BMMs (entry 1) to 2.29 for t-BMMs-APS (entry 2). This is due to inevitable partial dissolution of the unstable CTAB within t-BMMs-APS using toluene as the solvent, leading to the variations of the structural compactness. These results are also evident from the pore size distributions (as shown in Fig. 2a, and b) and the following demonstration of their TGA profiles (Fig. 6a, and b). As shown in Table 1 (entries 2 and 3), the fractal structure of P-t-BMMs (entry 3) was more compact than that of t-BMMs-APS (entry 2), due to larger  $D_m$  values of polymer-coated particles (2.39 for P-t-BMMs) than that of uncoated (2.29 for t-BMMs-APS). Therefore, these results indicate that the PAA macromolecules were potential to be successfully grafted on the surface of t-BMMs via covalent bonding. After further removal of CTAB from P-t-BMMs by extraction with NH<sub>4</sub>NO<sub>3</sub>/EtOH solvents, the  $D_m$  value of the obtained P-BMMs (entries 4) was about 2.32, smaller than that of P-t-BMMs ( $D_m = 2.39$ , entries 3). Obviously, the aforementioned behaviors almost conform to the change rule of fractal features. Moreover, as shown in Table 1 (entries 4 and 5), the  $D_m$  value slightly increased afterwards (from 2.32 (P-BMMs, entry 4) to 2.36 (P-Z@BMMs, entry 5)) following loading of Z, suggesting that their greater densifications when the Z were successfully loaded into the mesopores channels of the P-BMMs.

As a whole (as shown in Table 1, from entry 1 to entry 5), the  $D_m$  values of above samples gradually decreased from 2.50 (entry 1) to 2.36 (entry 5), which could be ascribed to successful grafting of PAA onto the surfaces of t-BMMs-APS, and the

**Table 1** Collections of the fractal dimension values, linear range, possible maximum particle dimensions, Porod deviation, and average interface layer thickness values of the related samples.

Entry	Sample	Slope <sup>[a]</sup>		Fractal dimension <sup>[a]</sup>		Linear range (nm <sup>-1</sup> )	Maximum Particle Size (nm) <sup>[b]</sup>	Porod deviation <sup>[c]</sup> average interface layer thickness values (nm) <sup>[d]</sup>
1	t-BMMs	-2.50	-3.71	$D_m = 2.50$	$D_s = 2.29$	$0.09 < q < 0.16$ $0.38 < q < 0.65$	53	Negative, 1.52
2	t-BMMs-APS	-2.29	-2.76	$D_m = 2.29$	$D_m = 2.76$	$0.09 < q < 0.16$ $0.38 < q < 0.65$	52	Negative, 1.48
3	P-t-BMMs	-2.39	-3.54	$D_m = 2.39$	$D_s = 2.46$	$0.09 < q < 0.16$ $0.38 < q < 0.65$	76	Positive, -
4	P-BMMs	-2.32	-2.95	$D_m = 2.32$	$D_m = 2.95$	$0.09 < q < 0.16$ $0.38 < q < 0.65$	61	Negative, 0.97
5	P-Z@BMMs	-2.36	-3.05	$D_m = 2.36$	$D_s = 2.95$	$0.09 < q < 0.16$ $0.38 < q < 0.65$	66	Positive, -

<sup>[a]</sup> Slopes between –1 and –3 refers to mass fractal structures (the mass fractal dimension,  $D_m = \alpha$ ,  $1 < D_m < 3$ ); slopes between –3 and –4 refers to surface fractal (the surface fractal dimension  $D_s = 6 - \alpha$ ,  $2 < D_s < 3$ ) (Hammersley et al., 2016; Xu et al., 2020; 2021; 2022a).

<sup>[b]</sup> Obtained from the PDDF analysis.

<sup>[c]</sup> Negative and positive deviation driving from Porod's law.

<sup>[d]</sup> The thickness values of an interfacial layer of the related samples were obtained by fitting the deviation directly, according to Porod's plots.

removal of CTAB within the mesoporous structures of p-t-BMMs, and the Z-loading inside the mesopore channels of P-BMMs. Besides, their behaviors possessed the fractal features ( $D_m$  or  $D_s$ ) in the high- $q$  region ( $0.38 < q < 0.65$ ), the situation with the fractal features appears to be more complicated, however, no obvious correlation of the above features is observed here, further consideration are therefore not considered.

Moreover, their detailed morphological information regarding the particle size, shape, and interfacial structures before and after modification could be derived from the PDDF profiles (Hammersley et al., 2016). As shown in Fig. 3B, judging from the shapes of all  $P(r) - r$  curves, as expected, all curves exhibited almost a symmetrical shape-form, the results suggested that the morphology of BMMs-based nanoparticles were approximately spherical, and changed unmarkedly after modification and loading, meanwhile, the following SEM images (as shown in Fig. 4) were also performed to support

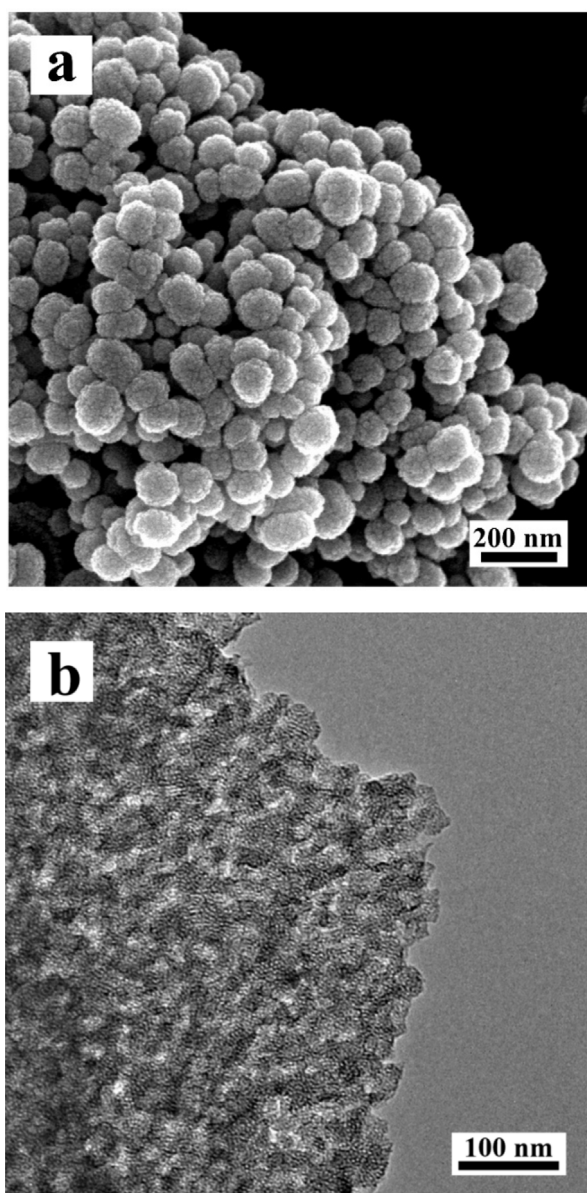
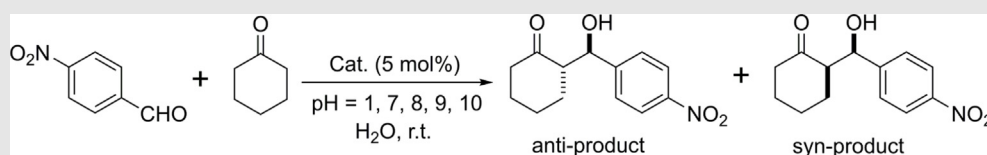


Fig. 4 (a) SEM and (b) TEM images of P-Z@BMMs.

the PDDF analysis. On the other hand, the intersections of these above curves and  $X$ -axis (as show in Fig. 3B, from -a to -e) denotes the maximum diameter ( $D_{max}$ ) of the nanoparticles (Hammersley et al., 2016), and the collections of the possible maximum particle sizes ( $D_{max}$ ) of the BMMs-based samples are listed in Table 1. As can be seen, the  $D_{max}$  of t-BMMs (Table 1, entry 1) was nearly the same as that of t-BMMs-APS (Table 1, entry 2), corresponding values were around 53 and 52 nm, respectively. These results indicate that the introduction of an amino group appears to have little effect on their particle size. However, the  $D_{max}$  became greater by PAA-grafting onto the surface of the t-BMMs, corresponding values increased from 52 nm for t-BMMs-APS (Table 1, entry 2) to 76 nm for P-t-BMMs (Table 1, entry 3), which were caused by the formation of amide bonds between the amino group of t-BMMs and the carboxylic group of PAA. These results implied that the PAA was successfully coated on the surfaces of t-BMMs, in well agreement with the demonstrations deriving from the fractal features. Furthermore, their  $D_{max}$  values decreased from 76 nm for P-t-BMMs (Table 1, entry 3) to 61 nm for P-BMMs (Table 1, entry 4) after removal of the template (CTAB), which should be attributed to the shrinkages of the silica frameworks. Comparably, further increases in particle size was observed after Z-loading, corresponding  $D_{max}$  values increased from 61 nm for P-BMMs (Table 1, entry 4) to 66 nm for P-Z@BMMs (Table 2, entry 5). Obviously, the enlarged particle size of P-Z@BMMs further indicated the Z-entering mesoporous channels of P-BMMs, being in good accordance with the demonstrations of the XRD patterns (as shown in Fig. 1). Besides, the sizes of P-Z@BMMs nanoparticles were also consistent with the estimated sizes by the following demonstration of the SEM images (as shown in Fig. 4).

In overall, the positive correlation between the fractal characteristics ( $D_m$ ) of the BMMs-based samples and their PDDF patterns were prominent, especially after PAA-grafting and subsequent Z-loading. As seen in Figure S2 of the ESI section, the scattering properties (including negative or positive deviation, as well as the average thickness of their interfacial layer) of the BMMs-based materials can be roughly estimated on the basis of Porod's law, their related structural parameters are collected in Table 1. As shown in Figure S2-A, the scattering curve ( $\ln[q^4 I(q)] \sim q^2$ ) of t-BMMs conformed well to Porod's law with a negative deviation, corresponding the thickness of an interfacial layer between the mesopores and silica matrix was around 1.52 nm (Table 1, entry 1). Herein, these results were a big difference from that of pure BMMs in the absence of CTAB according to the previous reported (Li et al., 2001; Xu et al., 2020; 2021; 2022a). As shown in Figure S2-B, the scattering curve of t-BMMs-APS also showed a negative deviation, corresponding values presented a decreased tendency from 1.52 nm (Table 1, entry 1) to 1.48 nm (Table 1, entry 2), which may be attributed to the decrease of an interface layer thickness due to the part removal of CTAB, being consistent with the fractal features and related PDDF analysis (as shown in Fig. 3). However, the Porod scattering of P-t-BMMs transformed from negative to positive deviation (as shown in Figure S2, from -B to -C), when achievement of the formation of the amide bonds on the surface of t-BMMs. In particular, we could speculate that the existences of the PAA layers caused significantly the additional scatterings, indicating the successful PAA-coating on the surfaces of t-

**Table 2** Aldol reaction results between *p*-nitrobenzaldehyde with cyclohexanone in the presence of P-Z@BMMs under different pH conditions.<sup>[a]</sup>

Entry	pH value	Yield <sup>[b]</sup> (%)	<i>dr</i> <sup>[c]</sup> (% anti/syn)	<i>ee</i> <sup>[c]</sup> (% anti)	TON	TOF [(gsh) <sup>-1</sup> ]
1	1.53	–	–	–	–	–
2	7.21	81.38	53:47	3.02	16.28	57.35
3	8.02	80.37	51:49	0.32	16.07	56.64
4	9.24	80.49	54:46	0.36	16.10	56.72
5	10.18	85.68	53:47	0.12	17.14	60.38

<sup>[a]</sup> Reaction conditions: *p*-nitrobenzaldehyde (0.1 mmol), cyclohexanone (1.0 mmol, 104.0  $\mu$ L), catalysts (5 mol%), H<sub>2</sub>O (0.5 mL), r.t., 120 h.

<sup>[b]</sup> Isolated yield after separation by silica gel.

<sup>[c]</sup> The diastereomeric and enantiomeric ratios were determined by chiral HPLC analysis.

BMMs. Subsequently, with the complete removal of CTAB from P-t-BMMs, the positive deviation would again be back to the negative deviation (as shown in Figure S2, from -C to -D), corresponding the thickness of an interfacial layer was around 0.97 nm (Table 1, entry 4). Comparably, its interface layer thickness was considerably smaller than that of t-BMMs-APS (1.48 nm, Table 1, entry 2), in other words, the average thickness of the grafted-PAA shell was estimated to be around 0.97 nm. Nevertheless, the scattering curve of P-Z@BMMs (Figure S2-E) conformed well to the results of the positive deviation from Porod's law after Z-loading with low amount, as described in Table 1 (entry 5). Thus, we speculate that the predominant reasons should be attributed to the additional scatterings deriving from Z-loading.

In conclusion, the comprehensive demonstrations on the basis of the XRD patterns, the N<sub>2</sub> sorption isotherms, and the SAXS analysis (including fractal evolution, PDDF profiles, and Porod plots) indicate the successfully uniformly PAA-coating on the outer-surface of the BMMs nanoparticles via covalent bonding, the Z species were also successfully loaded into the inner-mesoporous surface of the BMMs.

In order to fully and more accurately verify the above results, the following demonstrations of the SEM/TEM images, the dynamic light scattering (DLS) measurements, the elemental analysis, the FT-IR spectra, and the thermogravimetric (TG) profiles were robustly performed.

### 3.4. Sem/TEM images

The SEM and TEM images of P-Z@BMMs nanoparticles are shown in Fig. 4, the resultant nanoparticles were observed to have a nearly spherical morphology in size of around 70 nm with disordered and uniform distribution, similar to what we have previously reported results for parent BMMs or synthesized Z@BMMs (Sun et al., 2018; Tang et al., 2018; Xu et al., 2020; 2021; 2022a; Zhang et al., 2019). Besides, the mor-

phological features of the pH-sensitive catalysts are also well demonstrated on the basis of the N<sub>2</sub> sorption isotherms (as shown in Fig. 2e and Table 1 (entry 5) and PDDF profiles (Fig. 3B and Table 1 (entry 5)). However, the shell thickness of P-BMMs could not be visualized by the TEM image (Fig. 4b), because of too thin (probable < 1 nm) according to the comparison results of entry 3 and 4 in Table 1. In present work, the thickness of interfacial layer (PAA shell, around 0.97 nm) was estimated by Porod plot.

### 3.5. Dls measurements

The DLS measurements of related samples were also performed to support the SEM/TEM images and PDDF analysis, corresponding their apparent hydrodynamic diameter and polydispersity index (PDI) are summarized in Table S2. The mean particle sizes of samples obtained from the Gaussian fit of the histograms as shown in Fig. 5.

As can be seen in Table S2 (entries 1 and 2), the mean particle size of t-BMMs and t-BMMs-APS were around 531 and 397 nm, respectively. However, the size of P-t-BMMs increased greatly after PAA-grafting, up to a maximum of 1378 nm (Table S2, entry 3), indicating that the change rule of the hydrodynamic diameter was almost in line with that of PDDF analysis. Likewise, the apparent size measured by DLS was significantly larger than that measured by SEM/TEM (as shown in Fig. 4) due to hydration-induced expand of particles after soaking, originating from the existence of the PAA layers (Zayed et al., 2019) particularly for the swollen PAA networks at pH values higher than pK<sub>a</sub> (4.25). A detailed discussion regarding this phenomenon was explored in the following sensitivity analysis (as shown in Table 2). Besides, the mean particle sizes of P-BMMs (Table S2 (entry 4)) and P-Z@BMMs (Table S2 (entry 5)) were maintained at a relatively high level, further proving our reliable results.

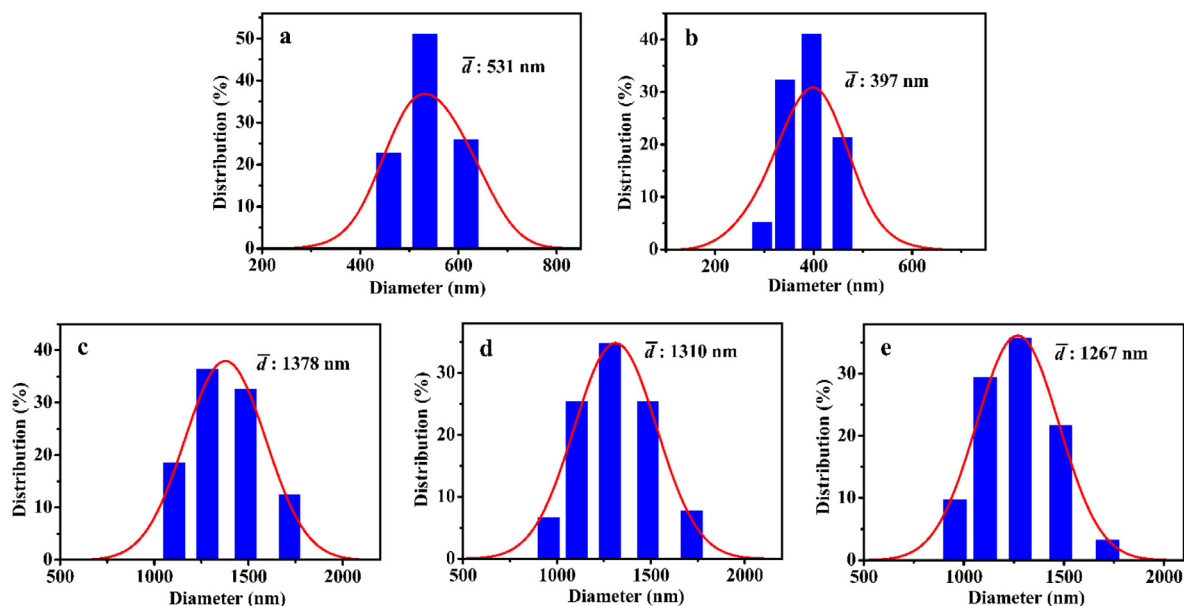


**Fig. 5** The hydrodynamic diameter distribution of (a) t-BMMs, (b) t-BMMs-APS, (c) P-t-BMMs, (d) P-BMMs, and (e) P-Z@BMMs.

As shown in [Table S2](#), the relative homogeneity of the BMMs-based nanoparticles can be roughly estimated by the PDI values, where the smaller the PDI values, suggesting a homogeneous and narrow particle size distribution. As a whole (from entries 1 to 5 in [Table S2](#)), their PDI values exhibited a trend of obvious decreasing during the surface modification, in which, PDI value of P-Z@BMMs was small of around 0.48, implying the homogeneous distributions of the particle and less tendency to agglomerate. Therefore, it can be concluded that the PAA-coated samples are considered as tend to mono-disperse, and the reliability of the conclusions inferred from the SEM/TEM images (as shown in [Fig. 4](#)) and PDDF profiles (as shown in [Fig. 3B](#) and [Table 1](#)) are also verified.

### 3.6. Tga profiles

The TG curves of all related samples are presented in [Fig. 6](#). As can be seen, the small weight loss at a temperature range of 30–200 °C was connected to the evaporation of physically or chemically adsorbed water and/or organic solvent on the surface of mesopores, whereas the gradual weight loss profiles of the BMMs-based samples from 200 to 900 °C were associated with the decompositions of the organic functional groups (amino, carboxyl, or amide), which is well agreement with the previous reports ([Sun et al., 2018](#); [Tang et al., 2018](#); [Xu et al., 2020](#); [2021](#); [2022a](#); [Zhang et al., 2019](#)).

Additionally, the TG profile of t-BMMs exhibited significantly weight loss of around 46.03 wt% (as shown in [Fig. 6a](#)), because of the CTAB decompositions. Herein, it was found that the weight loss of CTAB continues to decrease prior to the extracted with mixed solvents ([Fig. 6](#), from a to c), corresponding the weight loss values were around 32.12 wt% for t-BMMs-APS ([Fig. 6b](#)), and 22.73 wt% for P-t-BMMs ([Fig. 6c](#)), respectively, which may be attributed to the part removal of CTAB. These observations were consistent with the results of the XRD patterns (as shown in [Fig. 1](#)), N<sub>2</sub> sorption isotherms ([Fig. 2](#)), and SAXS analysis ([Fig. 3](#)). However,

the weight loss values increased from 20.06 wt% for P-BMMs ([Fig. 6d](#)) to 22.33 wt% for P-Z@BMMs ([Fig. 6e](#)). Indeed, these substantial alterations give rise to the formations of the interfacial thickness, the fractal evolution, as well as the variability in the pore sizes and porosity of nanoparticles. Consequently, these results indicate that the CTAB are almost completely removed via the solvents treatment, besides the successful Z-loading on the surfaces of mesopores.

### 3.7. Elemental analysis and FT-IR spectra

Furthermore, the elemental analysis results of N, C, and H in P-Z@BMMs are summarized in [Table S3](#). On the basis of the characteristic element (S) content, the Z-loaded amounts could be roughly estimated to around 2.97 wt% for P-Z@BMMs, in almost agreement with the results of TGA analysis (around 2.27 wt%).

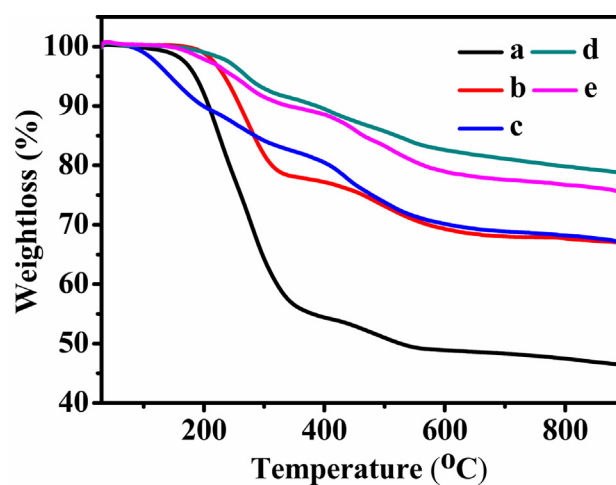


**Fig. 6** TG curves of (a) t-BMMs, (b) t-BMMs-APS, (c) P-t-BMMs, (d) P-BMMs, and (e) P-Z@BMMs.

As shown in Fig. 7, the FT-IR spectra were carried out to confirm the complete removal of CTAB and the successful PAA-coating on the surfaces of t-BMMs. As can be seen in Fig. 7a, the t-BMMs presented two intense peaks between 3000 and 2800  $\text{cm}^{-1}$ , which could be attributed to the asymmetric (2920  $\text{cm}^{-1}$ ) and symmetric (2850  $\text{cm}^{-1}$ ) stretching vibrations of the methylene chains, respectively (Quan et al., 2015). In particular, these intense peaks were also observed in prepared t-BMMs-APS (Fig. 7b) and P-t-BMMs (Fig. 7c), whereas almost absent in the extracted P-BMMs (Fig. 7d) or P-Z@BMMs (Fig. 7e), especially for the peak at 2920  $\text{cm}^{-1}$ , as supported by the almost complete removal of CTAB from the fabricated composite through extraction.

Besides, for P-t-BMMs, P-BMMs, and P-Z@BMMs (Fig. 7, from c to e), the additional band appeared at 1650  $\text{cm}^{-1}$  was associated with the stretching vibrations of amide (OC-NH) bonds, in addition, for P-t-BMMs (Fig. 7c), the intensity of the C-H bonds in carboxyl groups (-COOH) bending vibration at 1450  $\text{cm}^{-1}$  obvious decreased compared to PAA (Fig. 7f). Therefore, the FT-IR spectra strongly support our conclusion that an efficient the covalent attachment of PAA on the surfaces of BMMs via formation of OC-NH bonds between -COOH groups of PAA and -NH<sub>2</sub> groups on the t-BMMs (as shown in Scheme 1). Moreover, the other bands at 1068, 950, and 800  $\text{cm}^{-1}$  are characteristics of bending vibrations of Si-O bonds, and stretching vibrations of Si-OH and Si-O-Si bonds, respectively (Sun et al., 2018; Tang et al., 2018; Xu et al., 2020; 2021; 2022a; Zhang et al., 2019;). Especially for the active species (Z), Fig. 7g indicated that the main bands located at 1677, and 1500  $\text{cm}^{-1}$  could be attributed to the C = O and C = N stretching vibrations in the amide group, respectively, which predominantly originate from the pyridine rings (Xu et al., 2020; 2021; 2022a). The characteristic peak of C = O arising from PAA at around 1652  $\text{cm}^{-1}$  was unobvious due to the strong nearby vibrational absorption peak in the region. Notably, the peak at around 1384  $\text{cm}^{-1}$  in FT-IR spectra represented the nitrate anions stretching vibration of NH<sub>4</sub>NO<sub>3</sub> (as shown in Fig. 7d, and e). However, the above bands could not visibly judge the differences between the Z and P-Z@BMMs. Therefore, the suc-

cessful Z-loading was further elaborated in the discussions below.

### 3.8. Catalytic performances for asymmetric aldol reaction

In order to evaluate the pH-sensitivity of the grafted-PAA shells and the loaded-Z catalytic properties, the prepared P-Z@BMMs were used as the catalysts, their catalytic performances for asymmetric aldol reaction are explored under various pH (1.53, 7.21, 8.02, 9.24, and 10.18) media.

Meanwhile, reaction progress was monitored by TLC analysis (as shown in Scheme S2 in the ESI section). As shown in Scheme S2-b, the bands of aldol products at acid condition (pH = 1.53) were almost not reflected on TLC plates, similar to that of control group (only reactant: p-nitrobenzaldehyde, as shown in Scheme S2-a). However, as shown in Scheme S2-c, and -d, two bands of aldol products at neutral condition (pH = 7.21) and at alkaline condition (pH = 8.02) were observed on TLC plates, while the band of the reactant practically disappeared. Obviously, these observations further manifested that the PAA shell prevented the release of active species (Z) from P@BMMs matrix under acidic conditions, but promoted its release under neutral and alkaline conditions.

As shown in Table 2 (entry 1), a significant percentage of the unreacted substrates was observed despite in the presence of sufficient amounts (5 mol%) of P-Z@BMMs under the acid condition (pH = 1.53), and almost no reaction was occurred even after 120 h at room temperature. However, the reaction yield reached 80 % (Table 2 (entry 2-5)) under neutral or alkaline conditions (pH = 7.21, 8.02, 9.24 and 10.18), indicating that P-Z@BMMs had a high catalytic activity due to the Z-releasing from P-Z@BMMs. In particular, as mentioned above, the pK<sub>a</sub> of PAA is about 4.25. When P-Z@BMMs is in a low pH solution, the appearances of hydrogen bond leads to the shrinkage of the PAA shells with the dense networks, and the Z loaded in P-Z@BMMs is difficult to be released, showing a low catalytic activity. As increasing of pH values, the carboxyl groups in the PAA networks are ionized, causing the swelling of the PAA shell due to electrostatic repulsion. As a result, the PAA network channels were opened, and Z in P-Z@BMMs was easily released, showing a high catalytic activity. However, according to our previously published report, when Z or Z@BMMs were used as homogeneous or heterogeneous catalysts under the same acidic conditions, the desired product was obtained in 91% yield (Xu et al., 2020; 2022b). Therefore, as expected, the active species (Z) cannot be released from P-Z@BMMs for exerting catalytic effects due to their shrinkage of the PAA shell.

The TON and TOF values under the catalysis of P-Z@BMMs were provided in Table 2. In particular, the maximum TON and TOF values of the catalytic aldol reaction using p-nitrobenzaldehyde as substrate were calculated to be 17.14 and 60.38 [(gsh)<sup>-1</sup>] under the alkaline conditions (pH = 10.18).

Consequently, the resulting data strongly support our conclusions that the active species (Z) in P-Z@BMMs was hardly to be released under the acid solutions. Interestingly, this process further results in the controllable release of the active species (Z) by altering their acid-base systems. Nevertheless, it was found that the obtained yields, *dr*, and *ee* values were almost unchanged in a limited pH region (from 7 to 10, as shown in

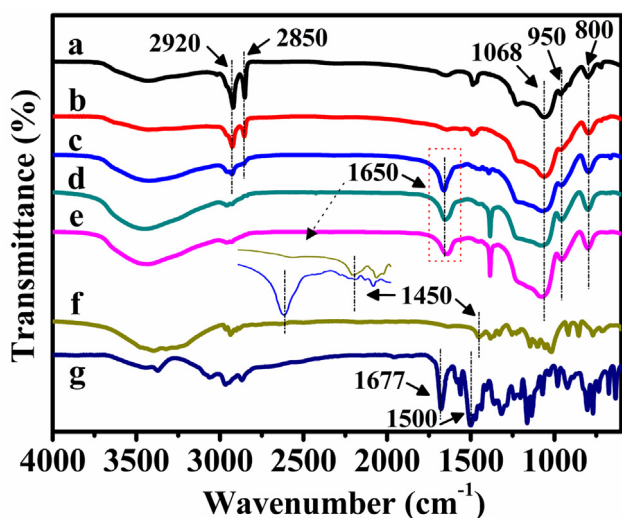


Fig. 7 FT-IR spectra of (a) t-BMMs, (b) t-BMMs-APS, (c) P-t-BMMs, (d) P-BMMs, (e) P-Z@BMMs, (f) PAA, and (g) Z.

Table 2 (entries 2–5)), these results indicate that the PAA shells of the P-Z@BMMs catalyst were insensitive to the above pH region. Overall, the controlled release of the active species (Z) from its protective P-BMMs coating can be achieved by simply adjusting pH values.

The possible catalytic mechanism between *p*-nitrobenzaldehyde (as an aldol acceptor) and cyclohexanone (as an aldol donor) was demonstrated in our previous reports (Xu et al., 2020; 2021).

#### 4. Conclusions

In summary, the PAA-coated Z@BMMs nanocomposites with core-shell structure were successfully synthesized using the BMMs as core and pH responsive PAA as a shell. Meanwhile, a pH-responsive release mechanism for asymmetric aldol reaction based on P-Z@BMMs were particularly proposed. In which, the PAA successfully covalently linked to the surfaces of amine-functionalized t-BMMs, their structural features and physicochemical properties were demonstrated thoroughly by SAXS patterns and other characterizations. In particular, the fractal evolutions, PDDF profiles, and Porod plots of the synthesized BMMs-based samples before and after modification suggested the successful PAA grafted onto the surfaces of BMMs, and Z loaded into the mesoporous channels, which was further corroborated by XRD patterns, N<sub>2</sub> sorption isotherms, SEM/TEM images, DLS measurements, TGA profiles, and FT-IR spectra. Meanwhile, their catalytic performance between *p*-nitrobenzaldehyde and cyclohexanone showed the Z species were successfully loaded into P-BMMs, and controlled release of loaded Z species were achieved by adjusting pH values. In particular, the synthesized P-Z@BMMs presented the satisfactory catalytic yields (around 80%) in comparison with the homogeneous catalytic system using Z as the catalysts. These results open perspectives to design appropriate surface-functionalized pH-sensitive catalysts for further use in asymmetric aldol reaction.

#### CRedit authorship contribution statement

**Guangpeng Xu:** Investigation, Writing – original draft, Data curation. **Bingying Jia:** Investigation, Writing – original draft, Data curation. **Bang Xu:** Supervision, Conceptualization, Methodology. **Shiyang Bai:** Formal analysis, Validation. **Jihong Sun:** Supervision, Conceptualization, Methodology. **Tallat Munir:** Formal analysis, Validation.

#### Declaration of Competing Interest

The authors declare that they have no known competing financial interests or personal relationships that could have appeared to influence the work reported in this paper.

#### Acknowledgements

This project was supported by the National Natural Science Foundation of China (21878006). We also gratefully acknowledge Dr Zhihong Li working at the Beijing Synchrotron Radiation Facility (BSRF) for a fruitful discussion on SAXS measurements and fractal dimension.

#### Appendix A. Supplementary data

Supplementary data to this article can be found online at <https://doi.org/10.1016/j.arabjc.2023.104933>.

#### References

- Alcaide, B., Almendros, P., 2002. The direct catalytic asymmetric aldol reaction. *Eur. J. Org. Chem.* 10, 1595–1601. [https://doi.org/10.1002/1099-0690\(200205\)2002:10<1595::AID-EJOC1595>3.0.CO;2-M](https://doi.org/10.1002/1099-0690(200205)2002:10<1595::AID-EJOC1595>3.0.CO;2-M).
- Bao, Y.M., Kumagai, N., Shibasaki, M., 2015. Managing the retro-pathway in direct catalytic asymmetric aldol reactions of thioamides. *Chem. Sci.* 6, 6124–6132. <https://doi.org/10.1039/C5SC02218E>.
- Calderón, F., Fernández, R., Sánchez, F., Fernández-Mayoralas, A., 2005. Asymmetric aldol reaction using immobilized proline on mesoporous support. *Adv. Synth. Catal.* 347, 1395–1403. <https://doi.org/10.1002/adsc.200505058>.
- Corma, A., 2016. Heterogeneous catalysis: Understanding for designing, and designing for applications. *Angew. Chem. Int. Ed.* 55, 6112–6113. <https://doi.org/10.1002/anie.201601231>.
- Dhar, D., Beadham, I., Chandrasekaran, S., 2003. Proline and benzylpenicillin derivatives grafted into mesoporous MCM-41: Novel organic-inorganic hybrid catalysts for direct aldol reaction. *J. Chem. Sci.* 115, 365–372. <https://doi.org/10.1007/BF02708229>.
- Doyagüez, E.G., Calderón, F., Sánchez, F., Fernández-Mayoralas, A., 2007. Asymmetric aldol reaction catalyzed by a heterogenized proline on a mesoporous support, The role of the nature of the solvents. *J. Org. Chem.* 72, 9353–9356. <https://doi.org/10.1021/jo070992s>.
- Esmailnejad-Ahranjani, P., Kazemeini, M., Singh, G., Arpanaei, A., 2016. Study of molecular conformation and activity-related properties of lipase immobilized onto core-shell structured polyacrylic acid-coated magnetic silica nanocomposite particles. *Langmuir*. 32, 3242–3252. <https://doi.org/10.1021/acs.langmuir.5b03614>.
- Gao, J.S., Liu, J., Jiang, D.M., Xiao, B., Yang, Q.H., 2009a. L-prolinamide functionalized mesoporous silicas: Synthesis and catalytic performance in direct aldol reaction. *J. Mol. Catal. A: Chem.* 313, 79–87. <https://doi.org/10.1016/j.molcata.2009.08.005>.
- Gao, Q., Xu, Y., Wu, D., Sun, Y.H., Li, X.A., 2009b. pH-responsive drug release from polymer-coated mesoporous silica spheres. *J. Phys. Chem. C*. 113, 12753–12758. <https://doi.org/10.1021/jp9043978>.
- Hammersley, A.P., 2016. FIT2D: a multi-purpose data reduction, analysis and visualization program. *J. Appl. Crystallogr.* 49, 646–652. <https://doi.org/10.1107/S1600576716000455>.
- Han, J., Sun, J.H., Bai, S.Y., Panzai, H., Jin, X.Q., Wu, X., 2015. “Graft to” synthesis and ibuprofen-loading performance of pH-sensitive PMAA-silica hybrid nanoparticles with controlled bimodal mesopores. *J. Pharm. Sci.* 104, 4299–4306. <https://doi.org/10.1002/jps.24668>.
- Hong, C.Y., Li, X., Pan, C.Y., 2009. Fabrication of smart nanocontainers with a mesoporous core and a pH-responsive shell for controlled uptake and release. *J. Mater. Chem.* 19, 5155–5160. <https://doi.org/10.1039/B820534E>.
- Hsiao, L.H., Chen, S.Y., Huang, S.J., Liu, S.B., Chen, P.H., Chan, C. C., Cheng, S., 2009. Enantioselective addition of diethylzinc to benzaldehyde over mesoporous SBA-15 functionalized with chiral proline derivatives. *Appl. Catal. A*. 359, 96–107. <https://doi.org/10.1016/j.apcata.2009.02.034>.
- Jin, X.Q., Wang, Q., Sun, J.H., Panzai, H., Bai, S.Y., Wu, X., 2018. P(NIPAM-co-AA)@BMMs with mesoporous silica core and controlled copolymer shell and its fractal for dual pH- and temperature-responsive performance of ibuprofen release. *Int. J. Polym. Mater. Polym. Biomater.* 7, 131–142. <https://doi.org/10.1080/00914037.2017.1309544>.
- Kutzscher, C., Nickerl, G., Senkovska, I., Bon, V., Kaskel, S., 2016. Proline functionalized UiO-67 and UiO-68 type metal-organic frameworks showing reversed diastereoselectivity in aldol addition reactions. *Chem. Mater.* 28, 2573–2580. <https://doi.org/10.1021/acs.chemmater.5b04575>.

- Li, Z.H., Gong, Y.J., Wu, D., Sun, Y.H., Wang, J., Liu, Y., Dong, B. Z., 2001. A negative deviation from Porod's law in SAXS of organo-MSU-X. *Micropor. Mesopor. Mat.* 46, 75–80. [https://doi.org/10.1016/S1387-1811\(01\)00292-X](https://doi.org/10.1016/S1387-1811(01)00292-X).
- Li, H., Pérez-Trujillo, M., Cattoën, X., Pleixats, R., 2019. Recyclable mesoporous organosilica nanoparticles derived from proline-valinol amides for asymmetric organocatalysis. *ACS Sustainable Chem. Eng.* 7, 14815–14828. <https://doi.org/10.1021/acssuschemeng.9b02838>.
- List, B., Lerner, R.A., Barbas, C.F., 2000. Proline-catalyzed direct asymmetric aldol reactions. *J. Am. Chem. Soc.* 122, 2395–2396. <https://doi.org/10.1021/ja994280y>.
- Lu, A., Smart, T.P., Epps, T.H., Longbottom, D.A., O'Reilly, R.K., 2011. L-proline functionalized polymers prepared by RAFT polymerization and their assemblies as supported organocatalysts. *Macromolecules.* 44, 7233–7241. <https://doi.org/10.1021/ma201256m>.
- Ma, J.Y., Sun, J.H., Fan, L., Bai, S.Y., Panezai, H., Jiao, Y.W., 2020. Fractal evolution of dual pH- and temperature-responsive P (NIPAM-co-AA)@BMMs with bimodal mesoporous silica core and coated-copolymer shell during drug delivery procedure via SAXS characterization. *Arabian J. Chem.* 13, 4147–4161. <https://doi.org/10.1016/j.arabj.2019.06.012>.
- Quan, G.L., Pan, X., Wang, Z.H., Wu, Q.L., Li, G., Dian, L.H., Chen, B., Wu, C.B., 2015. Lactosaminated mesoporous silica nanoparticles for asialoglycoprotein receptor targeted anticancer drug delivery. *J. Nanobiotechnol.* 13, 7. <https://doi.org/10.1186/s12951-015-0068-6>.
- Sánchez-Antonio, O., Romero-Sedglach, K.A., Vázquez-Orta, E.C., Juaristi, E., 2020. New mesoporous silica-supported organocatalysts based on (2S)-(1,2,4-triazol-3-yl)-proline: efficient, reusable, and heterogeneous catalysts for the asymmetric aldol reaction. *Molecules.* 25, 4532. <https://doi.org/10.3390/molecules25194532>.
- Sun, J.H., Zhang, Y.J., Bai, S.Y., Wu, X., Zhao, H.W., 2018. CN108295908A.
- Sun, J.H., Shan, Z.P., Maschmeyer, T., Coppens, M.O., 2003. Synthesis of bimodal nanostructured silicas with independently controlled small and large mesopore sizes. *Langmuir.* 19, 8395–8402. <https://doi.org/10.1021/la0351156>.
- Suzuki, K., Siddiqui, S., Chappell, C., Siddiqui, J.A., Ottenbrite, R. M., 2000. Modification of porous silica particles with poly(acrylic acid). *Polym. Adv. Technol.* 11, 92–97. [https://doi.org/10.1002/\(SICI\)1099-1581\(200002\)11:2<92::AID-PAT941>3.0.CO;2-W](https://doi.org/10.1002/(SICI)1099-1581(200002)11:2<92::AID-PAT941>3.0.CO;2-W).
- Svergun, D.I., Koch, M.H.J., 2003. Small-angle scattering studies of biological macromolecules in solution. *Rep. Prog. Phys.* 66, 1735–1782. <https://doi.org/10.1088/0034-4885/66/10/R05>.
- Tan, L., Yang, M.Y., Wu, H.X., Tang, Z.W., Xiao, J.Y., Liu, C.J., Zhuo, R.X., 2015. Glucose- and pH-responsive nanogated ensemble based on polymeric network capped mesoporous silica. *ACS Appl. Mater. Interfaces.* 7, 6310–6316. <https://doi.org/10.1021/acsaami.5b00631>.
- Tang, Z.Y., Sun, J.H., Zhao, H.W., Bai, S.Y., Wu, X., Panezai, H., 2018. Luminescent behaviors of bipyridine proline-grafted hybrid bimodal mesoporous silica and its catalytic performance in asymmetric aldol reaction. *Micropor. Mesopor. Mat.* 260, 245–252. <https://doi.org/10.1016/j.micromeso.2017.10.048>.
- Vishnumaya, M.R., Singh, V.K., 2009. Highly efficient small organic molecules for enantioselective direct aldol reaction in organic and aqueous media. *J. Org. Chem.* 74, 4289–4297. <https://doi.org/10.1021/jo900548f>.
- Wang, Q., Jin, X.Q., Sun, J.H., Bai, S.Y., Wu, X., 2017. PAA-grafted surface and fractal feature of dense nanosilica spheres for ibuprofen delivery. *Mater. Chem. Phys.* 195, 213–223. <https://doi.org/10.1016/j.matchemphys.2017.04.026>.
- Wang, C.E., Yan, Q., Liu, H.B., Zhou, X.H., Xiao, S.J., 2011. Different EDC/NHS activation mechanisms between PAA and PMAA brushes and the following amidation reactions. *Langmuir.* 27, 12058–12068. <https://doi.org/10.1021/la202267p>.
- Xu, G.P., Bing, L.J., Sun, J.H., Jia, B.Y., Bai, S.Y., 2021. Fractal features of the catalytic performances of bimodal mesoporous silica-supported organocatalysts derived from bipyridine-proline for asymmetric aldol reaction. *Asian J. Org. Chem.* 11, e202100631.
- Xu, G.P., Bing, L.J., Jia, B.Y., Bai, S.Y., Sun, J.H., 2022a. Comparison of mesoporous fractal characteristics of silica-supported organocatalysts derived from bipyridine-proline and resultant effects on catalytic asymmetric aldol performances. *RSC Adv.* 12, 10800–10814. <https://doi.org/10.1039/D2RA00971D>.
- Xu, X.H., Sun, J.H., Bing, L.J., Cui, X.Q., Jia, B.Y., Bai, S.Y., 2022b. Fractal features of dual temperature/pH-sensitive poly (N-isopropylacrylamide-co-acrylic acid) hydrogels and resultant effects on the controlled drug delivery performances. *Eur. Polym. J.* 171, <https://doi.org/10.1016/j.eurpolymj.2022.111203>.
- Xu, G.P., Zhang, Y.J., Sun, J.H., Bai, S.Y., Zhao, H.W., 2020. Synthesis of extended bipyridine-proline chiral catalysts and resulting effects on the asymmetric aldol reactions of bulkier aldehyde derivatives with cyclohexanone. *ChemistrySelect.* 5, 10996–11003. <https://doi.org/10.1002/slct.202002956>.
- Yan, J.C., Wang, L., 2009. Asymmetric aldol reactions catalyzed by efficient and recyclable silica-supported proline-based peptides. *Chirality.* 21, 413–420. <https://doi.org/10.1002/chir.20603>.
- Ye, L., Lay, C.L., 2013. Smart polymers functionalized hollow silica vesicles, US20130034609A1.
- Yuan, L., Tang, Q.Q., Yang, D., Zhang, J.Z., Zhang, F.Y., Hu, J.H., 2011. Preparation of pH-responsive mesoporous silica nanoparticles and their application in controlled drug delivery. *J. Phys. Chem. C.* 115, 9926–9932. <https://doi.org/10.1021/jp201053d>.
- Zayed, D.G., Ebrahim, S.M., Helmy, M.W., Khattab, S.N., Bahey-El-Din, M., Fang, J.Y., Elkhodairy, K.A., Elzoghby, A.O., 2019. Combining hydrophilic chemotherapy and hydrophobic phytotherapy via tumor-targeted albumin-QDs nano-hybrids: covalent coupling and phospholipid complexation approaches. *J. Nanobiotechnol.* 17, 7. <https://doi.org/10.1186/s12951-019-0445-7>.
- Zhang, Y.J., Sun, J.H., Bai, S.Y., Zhao, H.W., Wu, X., Panezai, H., 2019. Stability of immobilization of bipyridine-proline on Zn-modified bimodal mesoporous silicas and recyclable catalytic performance in asymmetric aldol reaction. *ChemistrySelect.* 4, 3105–3112. <https://doi.org/10.1002/slct.201804000>.
- Zhao, H.W., Li, H.L., Yue, Y.Y., Qin, X., Sheng, Z.H., Cui, J., Su, S., Song, X.Q., Yan, H., Zhong, R.G., 2012. Design, synthesis and use of novel 3,3'-disubstituted 2,2'-bipyridine-based chiral ligands: asymmetric catalysis in direct aldol reactions. *Synlett.* 23, 1990–1994. <https://doi.org/10.1055/s-0032-1316582>.
- Zhao, H.W., Li, H.L., Yue, Y.Y., Sheng, Z.H., 2013a. Diastereoselective and enantioselective michael addition reactions of ketones and aldehydes to nitro olefins catalyzed by C<sub>2</sub>-symmetric axially-unfixed biaryl-based organocatalysts derived from enantiopure  $\alpha$ -proline. *Eur. J. Org. Chem.* 9, 1740–1748. <https://doi.org/10.1002/ejoc.201201306>.
- Zhao, H.W., Yue, Y.Y., Li, H.L., Song, X.Q., Sheng, Z.H., Yang, Z., Meng, W., Yang, Z., 2013b. Novel axially unfixed biaryl-based water-compatible organocatalysts: Design, synthesis and their asymmetric catalysis in direct aldol reactions in water. *Synlett.* 24, 2160–2164. <https://doi.org/10.1055/s-0033-1339497>.
- Zhao, H.W., Yang, Z., Yue, Y.Y., Li, H.L., Song, X.Q., Sheng, Z.H., Meng, W., Guo, X.Y., 2014. Asymmetric direct michael reactions of cyclohexanone with aromatic nitroolefins in water catalyzed by novel axially unfixed biaryl-based bifunctional organocatalysts. *Synlett.* 25, 293–297.

- Zhou, L., Chu, B.F., Xu, X.Y., Xu, L., Liu, N., Wu, Z.Q., 2017. Significant improvement on enantioselectivity and diastereoselectivity of organocatalyzed asymmetric aldol reaction using helical polyisocyanides bearing proline pendants. *ACS Macro Lett.* 6, 824–829. <https://doi.org/10.1021/acsmacrolett.7b00439>.
- Zhou, J.M., Zhang, W.J., Hong, C.Y., Pan, C.Y., 2015. Silica nanotubes decorated by pH-responsive diblock copolymers for controlled drug release. *ACS Appl. Mater. Interfaces.* 7, 3618–3625. <https://doi.org/10.1021/am507832n>.